Facile Electrochemical Mg-ion Transport in a Defect-free Spinel Oxide

Bob Jin Kwon[1,2,], Liang Yin[2,3], Indrani Roy[2,4], Noel J. Leon[1,2], Khagesh Kumar[2,4], Jae Jin Kim[1,2], Jinhyup Han[1], Jihyeon Gim[1], Chen Liao[1,2], Saul H. Lapidus[2,3], Jordi Cabana[2,4], and Baris Key[1,2,*]*

[1]Chemical Sciences and Engineering Division Argonne National Laboratory, Lemont, IL 60439, United States

[2]Joint Center for Energy Storage Research, Argonne National Laboratory, Lemont, IL 60439, United States

[3]X-ray Science Division, Advanced Photon Source, Argonne National Laboratory, Lemont, IL, 60439, United States

[4]Department of Chemistry, University of Illinois at Chicago, Chicago, IL 60607, United States

Corresponding Author

*E-mail: bkwon@anl.gov, bkey@anl.gov

Abstract

Inversion, *i.e.* Mg/Mn antisite disorder, in a spinel oxide simultaneously causes blockage of favorable Mg^{2+} migration paths, raising activation barriers for diffusion, and it reduces the number of redox-active metals, limiting the maximum capacity in the spinel. An inversion-free spinel, $MgCr_{1.5}Mn_{0.5}O_4$, was synthesized by exploiting the different intrinsic crystal field stabilization of redox-active Cr and Mn in the form of a solid-solution. The capability of the tailored spinel to reversibly (de)intercalate Mg^{2+} at high redox potentials was investigated. The decrease in inversion dramatically lowered the electrochemical overpotential and hysteresis, and enabled utilization of high potentials at ~2.9 V (*vs*. Mg/Mg^{2+}) upon re-intercalation of Mg^{2+}. A combination of characterization techniques reveals that the structural, compositional, and redox changes within the spinel oxide were consistent with the observed electrochemical Mg^{2+} activity. Quantification of selective solely to lattice Mg^{2+} upon the electrochemical reaction was investigated by monitoring NMR signals in isotope ^{25}Mg enriched spinel oxides. Our findings enhance the understanding of Mg^{2+} transport within spinel oxide frameworks and provide conclusive evidence for bulk Mg migration in oxide lattices at high redox potentials with minimized electrochemical hysteresis.

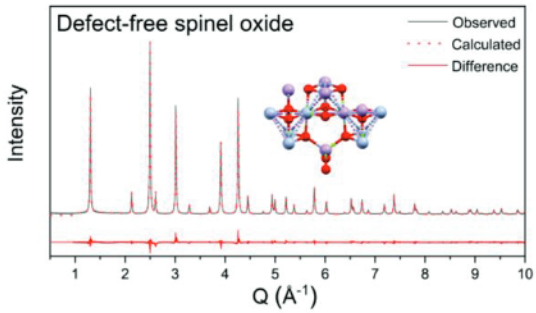

INTRODUCTION

Rechargeable Mg-ion batteries are considered as a potential alternative to state-of-the-art Li-ion batteries.[1-3] The success of Mg-ion batteries strongly depends on the discovery of functional cathodes with high capacities and operating potentials.[4-5] Up to now, reversible Mg^{2+} intercalation has been achieved in a few frameworks with soft anions (such as S^{2-} and Se^{2-})[6-8], albeit with low operating potentials (~1 V *vs.* Mg/Mg^{2+}). It severely limits the practical energy density, denoting the necessity of exploring new compounds operating at higher potentials. In theory, structures with ionic O^{2-} exhibit higher Mg^{2+} intercalation potentials than frameworks with soft anions, as evidenced by density functional theory (DFT) calculations.[9-10] On the other hand, oxide lattices are associated with poor Mg^{2+} diffusivity because of strong electrostatic cation-cation repulsion and cation-anion attraction in oxide lattices where the localized charges at Mg^{2+} and O^{2-} exist.[2] As a consequence, the slow migration of Mg^{2+} causes poor electrochemical properties and hysteresis along with considerably large overpotentials opening up undesired pathways for conversion of oxide cathodes and/or decomposition of electrolytes.[11-13] It is, therefore, crucial to design a functional oxide framework where Mg^{2+} (de)intercalates with suitable barriers and reversibly at high redox potentials in a non-aqueous electrolyte.

Oxide spinels are theoretically predicted to provide a favorable combination of capacity, operation potential, and cation mobility for a cathode material in a secondary Mg battery.[14-15] However, only a few spinel oxides (MgM_2O_4, M=Cr, V, Mn) have shown Mg^{2+} intercalation in non-aqueous electrolytes confirmed by evidence from secondary characterization.[14, 16-18] Specifically, the spinel framework with a Mn-redox center has been electrochemically successfully employed, whereas it was also observed that mobility and reversibility of Mg^{2+} were low along with considerable overpotentials even at high operating cell temperatures.[16-18] The origins of

issue were ascribed to complex factors including cation desolvation, charge transport at the interfaces, and crystallographic defects in the spinel oxide which must be addressed in order to enhance the kinetics of Mg^{2+}.[14, 19]

In a normal spinel structure (AB_2O_4, A: Mg^{2+}, B: transition metals), occupancy of tetrahedral rather than octahedral sites by Mg^{2+} promotes its diffusivity through a percolating network of 8*a*-16*c*-8*a* channels, which is a low-barrier migration path.[9] However, several studies on Mn-based spinels indicated susceptibility to inversion, *i.e.* Mg/Mn antisite disorder, where the octahedral sites (16*d*) are partially occupied by Mg^{2+} and Mn^{2+} partially occupies tetrahedral sites (8*a*), an occurrence that depends on the synthetic conditions and chemical compositions.[14, 20] These inverted configurations can arise depending on several competing factors, including the crystal field stabilization energies of the transition metals and entropic considerations.[21] The inversion is accompanied by the disproportionation of two Mn^{3+} (at 16*d* sites) into Mn^{2+} (at 8*a*) and Mn^{4+} (at 16*d*). Consequently, inversion causes a blockage of favorable Mg^{2+} percolation paths and limits the theoretically achievable capacity since only octahedral Mn^{+3} at 16*d* sites is redox active.[18, 20, 22]

Recently, bulk electrochemical Mg^{2+} activity with a notable degree of reversible intercalation using a tailored $MgCrMnO_4$ spinel was reported.[18] This composition in a form of solid-solution provided a suitable redox potential while moderate mobility was generated.[14, 18] It showed remarkable structural and electronic evolutions as a response to Mg^{2+} electrochemistry observed by multiple characterization techniques. On the other hand, significant overpotentials (> ~2 V) and electrochemical hysteresis still exist which induced reconstruction of oxide surfaces by over-magnesiation. The origin of the large overpotentials could be explained by the existence of Mg/Mn antisite disorder, as monitored by operando X-ray diffraction studies of the Mg^{2+} migration

mechanisms in the spinel.[22] The results indicated that Mg^{2+} migration is sensitive to structural disorder within the spinel lattice, which can be controlled *via* synthesis.[23]

In this work, a defect-free spinel oxide, $MgCr_{1.5}Mn_{0.5}O_4$ with ~1 % of inversion was synthesized. The capability of the tailored spinel to reversibly (de)intercalate Mg^{2+} at high potentials was investigated. Electrochemical overpotentials and hysteresis were lowered when the inversion defects were minimized in the spinels which enabled utilization of the high redox potential (~2.9 V *vs*. Mg/Mg^{2+}) for intercalating Mg^{2+}. X-ray diffraction, X-ray absorption spectroscopy and solid-state NMR revealed structural, compositional and redox changes in the oxides commensurate with the observed electrochemical activity. In particularly, quantification of lattice Mg^{2+} upon demagnesiation of the ^{25}Mg enriched spinel was achieved from its NMR signals in isotope enriched samples. Understanding the influence of inversion on electrochemical Mg^{2+} activity experimentally will provide a guideline to tailor architectures of the oxide spinels where Mg^{2+} intercalates reversibly with moderate migration barriers at high redox potentials. Finally, our findings emphasize the importance of design rules for a functional cathode to reach a critical milestone toward a high-energy Mg-ion battery.

EXPERIMENTAL SECTION

Synthesis

$MgCr_{2-x}Mn_xO_4$ spinels were synthesized by an aqueous sol-gel reaction, followed by annealing at 700 °C for 72 hours. Magnesium acetate tetrahydrate ($Mg(CH_3COO)_2 \cdot 4H_2O$, Product No. M5661 in Sigma-Aldrich), chromium acetate hydroxide ($Cr_3(CH_3CO_2)_7(OH)_2$, Product No.

318108 in Sigma-Aldrich), manganese acetate dihydrate ($Mn(CH_3COO)_3 \cdot 4H_2O$, Product No. 215880 in Sigma-Aldrich) were used as a precursor, and citric acid ($C_6H_8O_7$, Product No. C0759 in Sigma-Aldrich) was introduced as a chelating agent. The precursors in stoichiometric ratios, and citric acid were dissolved in 200 ml of deionized water and the solution was stirred vigorously for 30 minutes. The mixture was then heated at 120 °C to evaporate water until the powder was obtained. The powders were calcined at 700 °C for 72 hours in air. Post-annealed spinels were obtained by annealing as-made powders at 350 °C in air for a month, followed by quenching the annealed powders in liquid N_2. ^{25}Mg enriched spinels were synthesized by using ^{25}MgO (98% ^{25}Mg purity, MGLM-1335-PK, Cambridge Isotope Laboratories, Inc.) precursor as a source of Mg in the products instead of magnesium acetate tetrahydrate.

Characterizations

High-resolution synchrotron X-ray diffraction data were collected at 11-BM beamline at the Advanced Photon Source (APS), Argonne National Laboratory (ANL). Samples were loaded in Kapton capillaries and mounted on bases provided by the APS. Structures were refined using the Rietveld method as implemented in the TOPAS software package (Bruker-AXS, version 6) across a d-spacing range of 5.0 Å to 0.5 Å. Full-Width Half Maximum (FWHM) and Integral Breath (IB) based on volume-weighted column heights (LVol) were estimated by the macro function of "LVol FWHM CS G L" in TOPAS.

Solid-state ^{25}Mg magic angle spinning (MAS) NMR experiments were performed at 11.7 Tesla (500 MHz) on a Bruker Avance III spectrometer operating at a Larmor frequency of 30.64 MHz using a 3.2mm MAS probe. The spectra were acquired at a spinning speed of 20 kHz using

3.2mm rotors with a rotor synchronized spin-echo experiment (90°-τ-180°-τ) where τ is 1/r. All ^{25}Mg shifts were referenced to 5 M $MgCl_2$ (aq.) at 0 ppm. ^{25}Mg enriched (98% purity, MGLM-1335-PK) ^{25}MgO was purchased from Cambridge Isotope Laboratories, Inc.

Transmission electron microscopy (TEM) was carried out on a JEOL JEM 3010, operated at 300 kV. The images were analyzed to extract an average particle size by measuring ~100 particles using Image J from the Research Services Branch of NIMH & NINDS.

The electrochemical performance was evaluated on composites containing the $MgCr_{1.5}Mn_{0.5}O_4$ as working electrodes. Electrode slurries were prepared by mixing the active material, Timcal C45 carbon, and 6 wt% of a binder consisting of polyvinylidene difluoride (PVDF, Solvay) in N-methylpyrrolidone (NMP, Sigma-Aldrich) to make a dry electrode with a 5:3:2 ratio. Then, the slurry was cast on a stainless-steel foil, and it was dried under vacuum at 80 °C to evaporate NMP moiety overnight. The loading ratio (mg/cm^2) of active material in the dry electrodes was adapted to around 2 mg/cm^2. Circular pieces with a diameter of 3/8 inch were punched and assembled in coin cells in a glovebox filled with Ar gas where the levels of water and oxygen contents were below 1.0 ppm. Half-cell measurements were conducted in 0.5 M magnesium bis(trifluoromethylsulfonyl)imide ($Mg(TFSI)_2$, Solvionic, 99.5%) dissolved in 1-butyl-1-methylpyrrolidinium bis(trifluoromethylsulfonyl)imide (PY14TFSI, Solvionic, 99.9%)[24] or 0.1 M $Mg(TPFA)_2$ ($[TPFA]^- = [(Al(OC(CF_3)_3)_4)^-]$) dissolved in diglyme.[25] The electrolyte was dried at 120 °C under vacuum for 4 days until the water content was reduced to ~50 ppm. The counter electrode was an activated carbon cloth (ACC-5092-20, Kynol Co.), which was dried under vacuum at 110 °C overnight. Glass microfiber filters (VWR 28297-289) were used as separators in the coin cell experiment. Electrochemical measurements were performed on a MACCOR battery cycler at 95 °C. The potentials in this report are referenced to the activated

carbon cloth or Mg/Mg^{2+} couple depending on the cell configuration.[18, 24] The rate, *C/n*, was defined as the current density required to achieve a theoretical capacity of $MgCr_{1.5}Mn_{0.5}O_4$, C = 280 mAh/g, in *n* hours, assuming the reaction of $MgCr_{1.5}Mn_{0.5}O_4 \leftrightarrow Mg^{2+} + Cr_{1.5}Mn_{0.5}O_4$. Electrodes harvested for further characterization were washed multiple times with acetonitrile to remove electrolyte residues.

Mn K-edge X-ray absorption near-edge structure (XANES) was performed at the MRCAT insertion device beamline 10-ID at the Advanced Photon Source, Argonne National Laboratory (ANL). X-ray absorption spectra were collected in a transmission mode through the electrochemically treated ex-situ electrode laminates. Energy was scanned by a double-crystal Si (111) monochromator that was detuned by 50% and the incident and transmitted intensity was measured by gas ionization chambers. A Mn metal reference foil was measured simultaneously with each sample for energy calibration. Data analysis was completed using the IFEFFIT package. Mn $L_{II, III}$-edge X-ray absorption spectroscopy (XAS) measurements were carried out beamline 29-ID at Advanced Photon Source (APS) at Argonne National Laboratory (ANL, Lemont, IL). Cr $L_{II, III}$-edge X-ray absorption spectroscopy (XAS) measurements were carried out beamline 7-ID-1 at National Synchrotron Light Source II (NSLS-II) at Brookhaven National Laboratory (BNL, Upton, NY). To verify the electronic environment on the surface of the oxides, the Mn and Cr L-edge spectra were collected in a total electron yield (TEY) mode at room temperature and under ultra-high vacuum conditions (below 10^{-8} Torr). Contributions from visible light were carefully minimized before the acquisition, and all spectra were normalized by the current from freshly evaporated gold on a fine grid positioned upstream of the main chamber. The measured spectra were aligned by the beamline reference and a basic normalization using a linear background.

RESULTS AND DISCUSSION

1. Design and synthesis of a defect-free spinel oxide

A series of solid-solution, nanocrystalline $MgCr_{2-x}Mn_xO_4$, was synthesized *via* an aqueous sol-gel route followed by annealing at 700 °C in an air. Chemical compositions of Cr to Mn were controlled to preserve a cubic spinel lattice with a single phase. It was found that the highest achievable x for Mn in $MgCr_{2-x}Mn_xO_4$, was 1.0 while conserving a cubic spinel without any segregation of a secondary phase (Figure S1). It is worth noting that the cubic symmetry is observed even with high concentrations of Jahn-Teller active Mn^{3+}, due to preferential occupancy of Cr^{3+} in octahedral sites, suppressing the tetragonal distortion in the lattice. Above a 1:1 ratio of Cr to Mn in nominally $MgCrMnO_4$, a secondary phase was generated as shown in the powder diffraction data (Figure S1 and Table S1). The synchrotron diffraction patterns for all pristine $MgCr_{2-x}Mn_xO_4$ indicated a major cubic symmetry at a bulk scale. Different degrees of inversion, *i.e.* Mg/Mn antisite defects, were estimated by Rietveld refinement (Table S1). The inversion (*%*) in percentage is defined as the fraction of 8*a* sites occupied by Mn with a value of 0 % and 100 %, indicating a normal and a fully inverted spinel, respectively. The existence of Mg/Mn antisite defects not only raises the migration barriers of Mg^{2+} in the spinel oxides[20] but also decreases the number of utilizable redox-active Mn^{+3} at octahedral sites, denoting the necessity of tailoring an ideal spinel with zero defects.[14]

As shown in the diffraction patterns for the $MgCr_{2-x}Mn_xO_4$ series, increasing Cr contents lowered the inversion ratios in the spinel lattice (Figure S1 and Table S1). It was found that inversion ratios are inversely correlated to the theoretically achievable utilizable capacities.[20] For the Cr-rich composition, $MgCr_{1.5}Mn_{0.5}O_4$, the inversion ratio was significantly reduced to ~2 % where the majority of Mg^{2+} occupied tetrahedral sites, the lattice approaching ideal spinel

configuration. Furthermore, an attempt to reduce the antisite disorder was made by further post-annealing $MgCr_{1.5}Mn_{0.5}O_4$ powders for a month at 350 °C where a reported exothermic reaction takes place (The annealed product is referred as P-$MgCr_{1.5}Mn_{0.5}O_4$ throughout the manuscript).[26] Annealing at relatively low temperature induces structural reorganization, toward a thermodynamically stable configuration with lowered ratios of inversion.[26] The refinement of P-$MgCr_{1.5}Mn_{0.5}O_4$ indicated a further decrease of inversion (~1 %) without segregated new phases (Figure 1a). Therefore, the post-annealed spinel in this study, P-$MgCr_{1.5}Mn_{0.5}O_4$, represents a near-ideal spinel configuration approaching zero defects.

The nature of the local Mg^{2+} environments in $MgCr_{2-x}Mn_xO_4$ spinels was directly probed by solid-state ^{25}Mg MAS NMR (Figure 1b). The captured spectra provide Fermi contact shifts of ^{25}Mg depending on the ensemble of 1st and 2nd coordination shells Mg-O-Cr/Mn connectivity in the lattice due to the presence of paramagnetic centers in Cr^{3+} and Mn^{3+}, as well as $Mn^{2+/4+}$ created by Mg/Mn antisite defects.[18] Thus, it generates unique spectroscopic signatures for specific to lattice Mg^{2+} environments.[16, 27] In contrast, Fermi contact resonances, particularly for low gyromagnetic ratio quadrupolar nuclei such as ^{25}Mg, are typically broad because of the hyperfine coupling with unpaired electrons at 3*d* metals.[13] Due to the low natural abundance (~10%) of ^{25}Mg nuclei, the series of $MgCr_{2-x}Mn_xO_4$ spinels were also synthesized by using a ^{25}Mg isotope enriched precursor (^{25}MgO, 98% enrichment) to gain additional resolution of the individual lattice sites for Mg. Differences in phase purity, lattice parameters, and inversion ratios were observed in the refinements of the enriched materials (Figure S2 and Table S2). Compared to the non-enriched $MgCr_{2-x}Mn_xO_4$ (Table S1), enriched materials showed higher ratios of inversion, denoting the reaction sensitivity in the synthesis of Mn-based spinels (Table S2). Any deviations could be explained by a relatively less homogeneous sol-gel reaction when using insoluble ^{25}MgO instead

of $Mg(CH_3COO)_2$ as a source of Mg in the synthesis. As shown in Figure S3, a clear enhancement of the signal intensity at the same scan number was observed in the isotope enriched material.

The spectrum of pristine ^{25}Mg-enriched $MgCr_{1.5}Mn_{0.5}O_4$ containing ~10 % of inversion showed a symmetric resonance with a center of mass at ~2880 ppm with two sets of distinguishable spinning sidebands (Figure 1b). In the spinel structure, one tetrahedral Mg^{2+} is surrounded by 12 octahedral metals through coordination by oxygen anions.[14] In isotope enriched $MgCr_{1.5}Mn_{0.5}O_4$, ^{25}Mg hyperfine shifts are proportional to the number of such chemical contacts with 9 Cr and 3 Mn.[16] Considering the degree of paramagnetic shifts of ^{25}Mg in a single B-site spinel, $MgCr_2O_4$ (~2820 ppm, 1 Mg^{2+}-12 Cr^{3+}, ~235 ppm per Cr^{3+}) and $MgMn_2O_4$ (~3070 ppm, 1Mg^{2+}-12 Mn^{3+}, ~256 ppm per Mn^{3+}), the center of resonance at ~2880 ppm is consistent with local domains of Mg^{2+} coordinated to $9Cr^{3+}/3Mn^{3+}$ [(9×2820 + 3×3070)ppm ⁄ 12]No other distinct paramagnetic resonances from Fermi contacts exclusively between Mg^{2+} and Cr^{3+} or Mg^{2+} and Mn^{3+} were detected at 2820 ppm and 3070 ppm respectively[18], indicating no presence of locally segregated clusters. Therefore, the spectrum suggests complete Cr/Mn miscibility within the lattice and in the form of a solid-solution. On the other hand, distinct resonances were detected at precisely at +/- 140 ppm from 2880 ppm (at 3020 ppm and 2740 ppm), presumably due to presence of $Mn^{2+/4+}$ and Mg in octahedral 16*d* sites (Figure S4). The ratio of the total intensity of these sites was found to be ~10 % of the total Mg intensity in the sample and is consistent with the inversion ratio (~10 %) estimated by X-ray diffraction refinement (Figure S4 and Table S2).

Other ^{25}Mg-enriched cubic spinels with more Mn contents and inversion ratios were also synthesized (Figure S2 and Table S2). Compared to Cr-rich $MgCr_{1.5}Mn_{0.5}O_4$, the spectra of $MgCrMnO_4$ and $MgCr_{0.8}Mn_{1.2}O_4$ (Figure 1b) showed additional broadening, due to a wider range of random Cr/Mn local orderings around Mg and by the existence of significant $Mn^{2+/4+}$antisite

defects causing considerable overlap with the spinning sideband envelopes.[14, 27] When additional Mn was incorporated in the spinel, *i.e.* Mn-rich $MgCr_{0.8}Mn_{1.2}O_4$, an additional slight asymmetry towards higher frequencies was observed in the NMR signal (Figure S5). This is probably associated with the effect of randomization and the possibility that there is a higher probability of finding Mn around Mg in the Mn-rich spinel. Overall, the long- and short-range order characterization data was found to be highly consistent with the statistical Cr/Mn distribution around Mg and the extent of inversion defects in the structures.

2. Enhancement of electrochemical response for intercalation of Mg^{2+} by reducing inversion defects

The electrochemical properties were measured at 95 °C in a Mg half-cell consisting of a carbon cloth as a counter electrode and P-$MgCr_{1.5}Mn_{0.5}O_4$ containing ~1 % inversion as a working electrode with an ionic liquid electrolyte, $Mg(TFSI)_2$-PY14TFSI which has previously shown sufficient thermal and anodic stability for high-temperature electrochemistry (Figure 2a).[17, 24] The high surface area of the carbon cloth gives sufficient double layers of charges needed to operate with the positive electrode, the capacity being completely capacitive.[28] The cell was galvanostatically charged up to 1.4 V (*vs.* carbon) at a rate of C/50 which is calibrated to a potential of ~3.6 V *vs.* Mg/Mg^{2+} following procedures in the literature.[24] The cut-off potential was set to utilize a redox couple of $Mn^{3+/4+}$, owing to the high potential (≥ 3.6 V *vs.* Mg/Mg^{2+}) for oxidation of Cr^{3+}.[15, 18, 20] The charge profile was found to be sloping, centered at ~1.2 V *vs.* carbon (~3.4 V *vs.* Mg/Mg^{2+}, Figure 2a). A charging capacity of ~56 mAh/g was achieved at 1.4 V (*vs.* carbon). The charge capacity corresponds to approximately 0.2 moles of Mg^{2+} equivalents reacting per

mole of $MgCr_{1.5}Mn_{0.5}O_4$. Subsequently, the cell was discharged to -0.4 V *vs.* carbon (~1.8 V *vs.* Mg/Mg^{2+}) at a rate of C/50 and ~50 mAh/g of discharge capacity was achieved.

Another cell was prepared with the isotope enriched $MgCr_{1.5}Mn_{0.5}O_4$ containing ~10 % inversion defects, designed for ^{25}Mg NMR analysis (Figure 1b and Table S2). The test was intended to compare the electrochemical Mg^{2+} activities and voltage profiles when the concentration of antisite defects varies in the same composition (Figure 2a). A notable decrease in charge capacity (~29 mAh/g) was observed upon charging to 1.4 V (*vs.* carbon) when compared with the nearly zero inverted spinel. Upon subsequent discharge to -0.4 V (*vs.* carbon), ~38 mAh/g of capacity was achieved. Compared with P-$MgCr_{1.5}Mn_{0.5}O_4$ approaching zero inversion, a decrease in capacities of ~14 mAh/g was observed along with a relatively steep decline of the cathodic curve and larger overpotential for reintercalation, *i.e.,* greater electrochemical hysteresis (Figure 2a). The high electrochemical plateau at ~0.7 V *vs.* carbon (~2.9 V *vs.* Mg/Mg^{2+}) for reintercalation of Mg^{2+} detected in P-$MgCr_{1.5}Mn_{0.5}O_4$ cell was not clearly observed.

As shown in the *d*q/*d*v plot for P-$MgCr_{1.5}Mn_{0.5}O_4$ (Figure 2b), a dominant potential for reintercalation of Mg^{2+} appeared at ~0.7 V *vs.* carbon, converted to ~2.9 V (*vs.* Mg/Mg^{2+}), consistent with the redox $Mn^{3+/4+}$ potential in oxide spinels as theoretically predicted.[18] On the other hand, the *d*q/*d*v plot for the spinel $MgCr_{1.5}Mn_{0.5}O_4$ containing a higher inversion ratio indicated a notable increase in overpotentials and hysteresis with less electrochemical Mg activity. The possible effect on electrochemistry by a length of Mg diffusion across a particle were investigated by measuring sizes of multiple particles in transmission electron microscopy (Figure S6). Minor difference with ~4 nm in particle sizes between the two $MgCr_{1.5}Mn_{0.5}O_4$ containing different contents of inversion (~1 % *vs.* ~10 %) was observed. It implies that the length of diffusion through an individual particle was not a critical factor in the electrochemical properties.

The distinct profiles revealed a detrimental effect of structural defects in the electrochemical Mg activity, denoting the importance of tailoring structural configuration.

A similar electrochemical response was achieved in a Mg half-cell configuration with an alternative state-of-the-art electrolyte,[25] $Mg(TPFA)_2$ dissolved in diglyme (Figure S7a), highlighting its versatility. The capability in average potentials for Mg^{2+} intercalation was striking when comparing with the electrochemical profiles of $MgCrMnO_4$ (~16 % of inversion), and post-annealed $MgCrMnO_4$ (~10 % of inversion) cycled at the same electrochemical conditions in our previous work.[18] Defect minimized P-$MgCr_{1.5}Mn_{0.5}O_4$ (~1 % of inversion) in this work showed a higher average potential with an increase of ~0.4 V along with the enhanced discharge potential for Mg^{2+} re-intercalation. The cycling curve of P-$MgCr_{1.5}Mn_{0.5}O_4$ showed a decrease in capacity, to ~40 mAh/g after five cycles, then discharge capacities were relatively constant up to 50 cycles (Figure S7b).

3. Lattice breathing and quantification of lattice Mg^{2+} *via ss*-NMR

Synchrotron X-ray diffraction was measured from the electrodes at key states to gain insight into the structural evolution as a response to electrochemical Mg^{2+} (de)intercalation (Figure 3a and b). Diffraction of the charged electrode showed a notable shift of peaks to higher angles in all planes of the cubic P-$MgCr_{1.5}Mn_{0.5}O_4$ compared to the pristine state, indicating a decrease of the unit cell volume (Table S3). The lattice parameter of the pristine, 8.34362(5) Å, was significantly contracted to 8.31697(5) Å in the charged oxide, while no formation of secondary phase(s) *via* conversion reactions were detected. Moreover, a decrease in the ratio of intensities between (*111*) and (*311*) reflections was observed, correlating to the decrease in the number of

occupancies at tetrahedral Mg^{2+} sites, consistent with the observations in other spinels (Figure S8).[14, 18]

The tetrahedral sites emptied by Mg^{2+} deintercalation were quantified by X-ray Rietveld refinement (Figure S9), assuming that the inverted octahedral Mg^{2+} and tetrahedral Mn^{2+} were immobile under the electrochemical potentials, as recently proved by theoretical calculation and experimental operando study.[14, 22] The refinement indicated that ~0.19 mols of Mg^{2+} were deintercalated from the spinel (Table 1). It was consistent with deintercalated Mg^{2+} mols (~0.2 mols) estimated by the charge capacity (~56 mAh/g) delivered in the cell. Upon discharge with ~50 mAh/g of capacity, the diffraction peaks were reverted to lower angles consistent with remagnesiation and reversible intercalation behavior. Interestingly, the peak positions move slightly past the pristine state due to an additional increase of lattice volume. (Figure 3a and b). The lattice parameter of the discharged oxide was 8.35220(6) Å (Table S3), larger than pristine, suggesting a slight over-magnesiation. As indicated in the refinement of the remagnesiated state (Figure S9b and Table 1), the Mg^{2+} occupied two sites, the main tetrahedral 8*a* (~0.98 mols) and additional octahedral 16*c* sites (~0.016 mols) consistent with recent findings.[18, 22] It was found that the excess octahedral Mg^{2+} at 16*c* site was detrimental to its structural reversibility and diffusivity of Mg^{2+}.[22] The portion of octahedral Mg^{2+} at 16*c* sites (0.016 mols) in the discharged P-$MgCr_{1.5}Mn_{0.5}O_4$ was notably smaller than the occupancy (0.160 mols) observed in $MgCrMnO_4$, which contains a notable level of inversion with ~16 % in our previous study.[18, 22] This observation could be correlated to the existence of inversion in the spinel oxides.

The specific amount of deintercalated lattice Mg^{2+} only upon charge was further quantified by *ss*-NMR spin counting experiments with an isotope ^{25}Mg enriched spinel, $MgCr_{1.5}Mn_{0.5}O_4$ containing ~10 % of inversion (Figure 3c and Table S2). The ^{25}Mg enriched spinel was assembled

with a carbon cloth in the ionic liquid electrolyte. The cell was galvanostatically charged up to 1.5 V (*vs.* carbon) at a rate of C/100 at 95 °C, where theoretically extractable capacities, ~60 mAh/g, were delivered for enriched $MgCr_{1.5}Mn_{0.5}O_4$ (Figure S10). Normalized spectra for pristine and charged $MgCr_{1.5}Mn_{0.5}O_4$ are shown in Figure 3c in order to clearly reflect the degree of deintercalation of Mg^{2+}. Upon the anodic reaction, a major loss of intensity in the paramagnetic resonance, representative of lattice Mg, was detected with no distinct shifts. It showed roughly 0.25 mols of Mg^{2+} were deintercalated from the pristine state, similar with the theoretically extractable Mg^{2+} (~0.2 mols) as considering the ratio of inversion (~10 %) in pristine enriched $MgCr_{1.5}Mn_{0.5}O_4$ spinel.

4. Valence state changes at Mn and Cr upon (de)intercalation of Mg^{2+}

Mn K-edge X-ray absorption spectroscopy (XAS) was employed to understand the evolution of the electronic environment in P-$MgCr_{1.5}Mn_{0.5}O_4$ in response to Mg^{2+} (de)intercalation.[18, 29] The main absorption edge involves electronic transitions dominated by the promotion of electrons from an occupied 1*s* level to empty valence 4*p* bands, followed by higher transitions and the ionization threshold. Therefore, the position of the absorption white line is susceptible to changes in the effective charge at the Mn centers, which enables an estimation of the formal oxidation state of the ensemble average. Figure 4a presents normalized spectra for pristine, charged, and discharged non-enriched P-$MgCr_{1.5}Mn_{0.5}O_4$ (~1 % of inversion) electrodes prepared in a half-cell at 95 °C (Figure 2a). It is worth to noting that given the composition, P-$MgCr_{1.5}Mn_{0.5}O_4$ with ~1 % of inversion, the 0.49 mols of Mn in octahedral sites per mol of $MgCr_{1.5}Mn_{0.5}O_4$ are assumed as the centers for charge compensation within the applied potential window. The integration method was used to determine the position of the absorption edge of each

Mn K-edge spectra (Figure S11).[30] The estimated edge positions are summarized in Table S4. Compared with the values of Mn oxide standards in the literature, the bulk oxidation state of pristine was close to around +3 (Figure 4a and Table S4).[30] Upon the anodic reaction, the valence of Mn in the bulk was oxidized, as manifested by a shift of the main edge toward higher energy with ~0.42 eV (Figure 4a). The valence state of Mn at the charged P-$MgCr_{1.5}Mn_{0.5}O_4$ was estimated by comparing it with standard spinel $LiMn_2O_4$, which has an average oxidation state of Mn with +3.5 (Figure S11 and Table S4). The spectra showed a main edge at ~6550.55 eV, which is higher in energy than the edge position at ~6550.22 eV observed in the charged P-$MgCr_{1.5}Mn_{0.5}O_4$ (Figure S11 and Table S4). The comparison implies that the oxidation state of the charged electrode was slightly lower than +3.5. The main edge of the discharged state nearly shifted back to the initial position, denoting its reversibility in Mn valence states at the bulk. Reversible changes for Mn redox centers supported the bulk Mg^{2+} activity throughout the electrode, consistent with the X-ray diffraction analysis.

Mn L-edge spectra were collected in a total electron yielding (TEY) mode, which is sensitive to a ~5 nm depth, providing information on the chemical state of Mn at the surface of the electrode (Figure 4b). The L_{II} and L_{III} edges are captured from electronic transitions to the 3*d* bands from the $2p_{1/2}$ and $2p_{3/2}$ levels, respectively.[31] The alteration of the multiplet structure is attributed to the crystal symmetry at the ground state, whereas the shifts in center of gravity again reflect the changes in the formal oxidation states of Mn. P-$MgCr_{1.5}Mn_{0.5}O_4$ presented peaks of absorption at ~641.6, 643.3 and 644.6 eV, which can be associated with the dominant signals in the complex spectra of Mn^{2+}, Mn^{3+} and Mn^{4+}. The Mn^{2+} and Mn^{4+} are likely located at tetrahedral sites (8*a*) and octahedral sites (16*d*) in the spinel structure on the surface of particles, respectively which could be generated by the mechanism of Mn^{3+} disproportionation.[32] Upon the charge in a half-

there was an increase in relative intensity at 644.6 eV, indicating an increase in Mn^{4+} by oxidation of Mn^{3+} (Figure 4b and S12). Moreover, the branching ratio, I (L_{III}) / I (L_{III} + L_{II}), was decreased from 0.687 to 0.653 (Figure 4b). The smaller branching ratio indicates that the electronic environment evolved toward a lower spin state of Mn ions, as it occurs upon oxidation due to an overall decrease in unpaired electrons. After the cathodic reaction, the signatures associated with both Mn^{3+} and Mn^{4+} were notably weakened, revealing a reduction of Mn. Compared to the spectra of pristine, it showed more reduced Mn valence states (Figure S12), possibly due to excess magnesiation on the surface.[18]

The valence states of Cr at the surface of the pristine and charged P-$MgCr_{1.5}Mn_{0.5}O_4$ were identified by Cr L-edge XAS collected in a TEY mode (Figure 4c). The edges directly probe unfilled 3*d* states through the promotion of 2*p* electrons.[31] The pristine spectra presented intense absorption features at ~577.1 and ~578.4 eV in L_{III} edge and ~586.3 and ~587.9 eV in L_{II} edge, which can be associated with the expected octahedral Cr^{3+} due to the $3d^3$ configuration.[33] No peak shifts, indicative of changes in Cr valence state,[34-35] were observed in the charged state of P-$MgCr_{1.5}Mn_{0.5}O_4$ but rather a minor decrease in peak intensities at ~577.1 and 587.9 eV. Since the electrochemical potential for the anodic reaction was never reached to the predicted potentials of $Cr^{3+/4+}$,[15] the unchanged Cr valence state was a reasonable consequence. On the other hand, the changes in the intensities implied that there might have been minor alterations in local coordination around Cr owing to the oxidized Mn and deintercalated Mg^{2+}.

CONCLUSION

In this study, inversion-free spinel $MgCr_{1.5}Mn_{0.5}O_4$ was successfully synthesized. The tailored spinel showed reversible (de)intercalation of Mg^{2+} at high redox potentials. It was found that the overpotentials and, thus, overall hysteresis was reduced when the inversion ratio in the spinel lattice was minimized. Multimodal characterization by X-ray diffraction, X-ray absorption spectroscopy, and solid-state NMR indicated that structural, compositional, and redox changes were consistent with the observed electrochemical Mg^{2+} activity in the spinel oxide. An attempt to estimate deintercalated Mg^{2+} solely from the lattice was made by synthesizing ^{25}Mg isotope enriched $MgCr_{1.5}Mn_{0.5}O_4$, revealing approximately 0.25 mol Mg^{2+} were removed upon charge. Bulk redox changes at Mn were detected upon (de)intercalation of Mg^{2+}, whereas the valence state of Cr was unchanged. The experimental evidence emphasizes the influence of structural defects, in this case inversion, on electrochemical Mg^{2+} activity and provides a design rule toward a building functional Mg cathode for a high-energy Mg-ion battery.

Supporting Information

Supporting Information is available from of charge on the ACS Publication website. The file contains additional data discussed in the manuscript, collected by HE-XRD, ss-NMR, battery cycler, and XAS.

Corresponding Author

*Email: bkwon@anl.gov, bkey@anl.gov

Notes

The authors declare no conflict of interests.

Acknowledgements

This work was intellectually led and primarily supported by the Joint Center for Energy Storage Research (JCESR), and Energy Innovation Hub funded by the U.S. Department of Energy (DOE), Office of Science, Basic Energy Sciences. Use of the Advanced Photon Source at Argonne National Laboratory was supported by the U.S. Department of Energy, Office of Science, Office of Basic Energy Sciences, under Contract No. DE-AC02-06CH11357. IR and KK acknowledge support by National Science Foundation, under grants DMR-1809372 and CBET-18000357, respectively. This research used resources of the National Synchrotron Light Source II at 7-ID-1, a U.S. Department of Energy (DOE) Office of Science User Facility operated for the DOE Office of Science by Brookhaven National Laboratory under Contract No. DE-SC0012704.

FIGURES

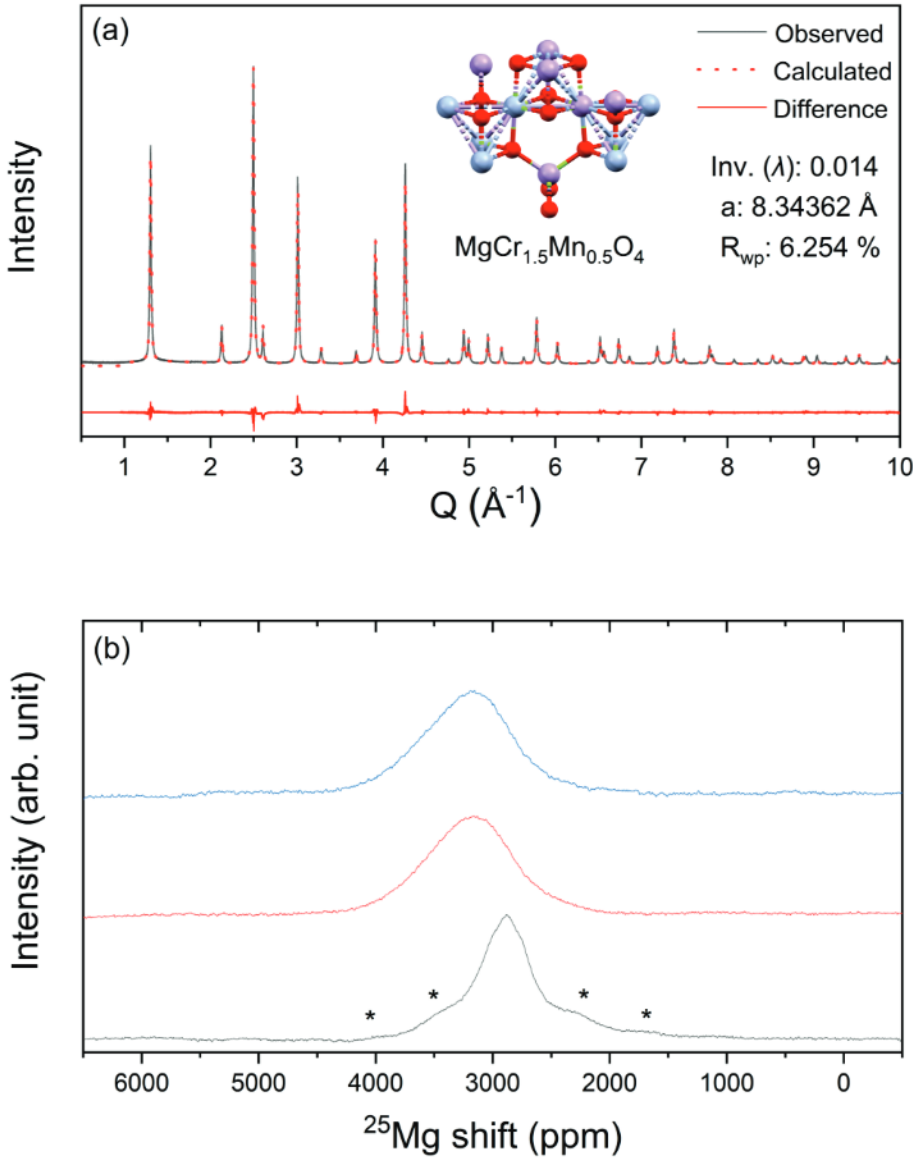

Figure 1. Synchrotron XRD patterns of (a) P-$MgCr_{1.5}Mn_{0.5}O_4$ and (b) solid-state NMR spectra of ^{25}Mg isotope enriched $MgCr_{1.5}Mn_{0.5}O_4$ (black), $MgCrMnO_4$ (red), and $MgCr_{0.8}Mn_{1.2}O_4$ (blue). Asterisk marks indicate spinning side bands.

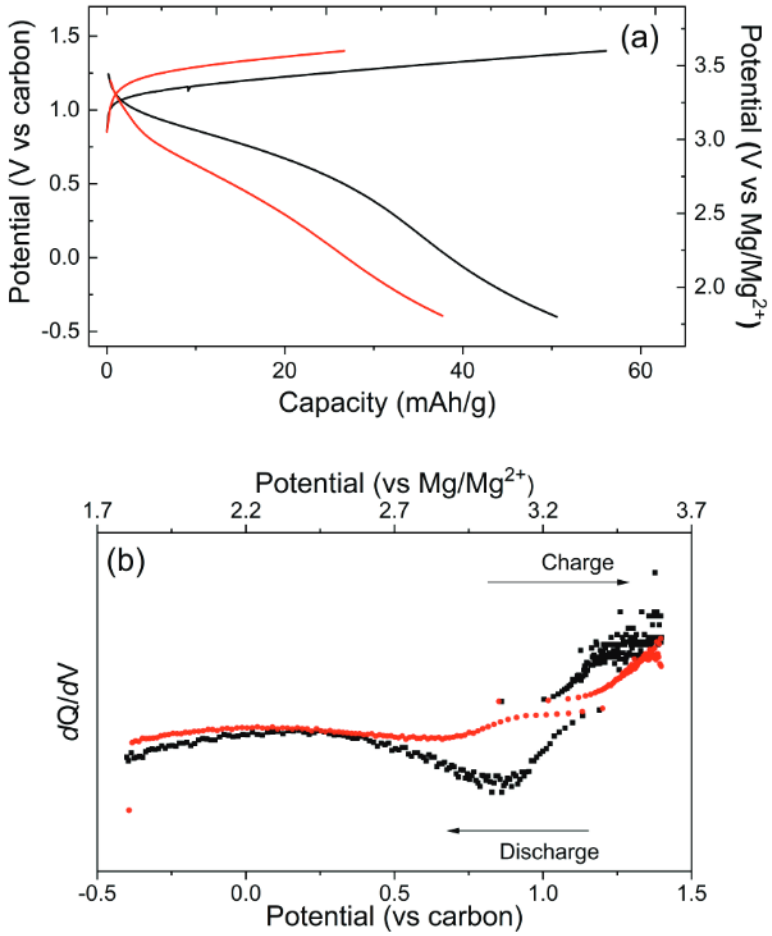

Figure 2. (a) Representative potential versus capacity profile and (b) the corresponding *d*q/*d*v plots of P-$MgCr_{1.5}Mn_{0.5}O_4$ (~1 % of inversion, black) and isotope enriched $MgCr_{1.5}Mn_{0.5}O_4$ (~10 % of inversion, red) measured in a coin cell at 95 °C in $Mg(TFSI)_2$-PY14TFSI electrolyte.

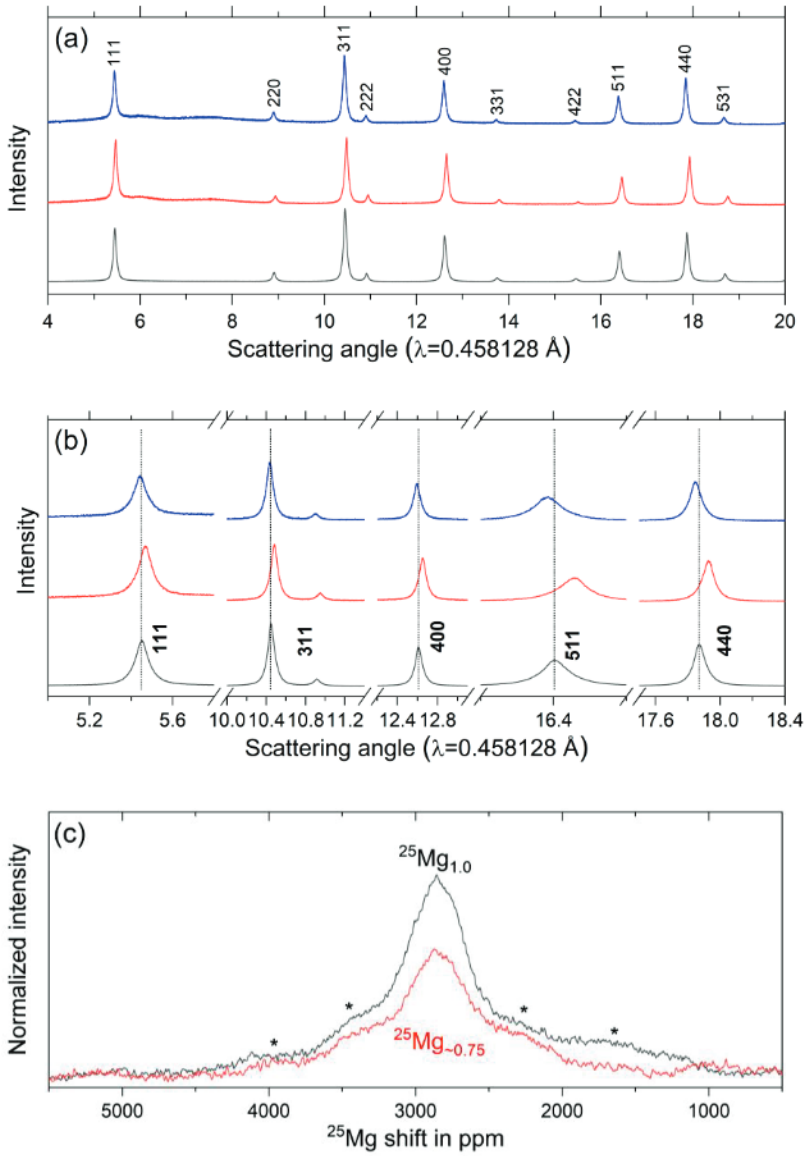

Figure 3. Synchrotron XRD patterns of pristine (black), charged (red), and discharged (blue) P-$MgCr_{1.5}Mn_{0.5}O_4$ electrode powders in (a) wide and (b) zoom-in angles. (c) Normalized solid-state NMR spectra of pristine (black) and charged (red) ^{25}Mg enriched $MgCr_{1.5}Mn_{0.5}O_4$. The spectra were normalized by the number of scans and sample weights.

Table 1. Structural information of pristine, charged and discharged P-$MgCr_{1.5}Mn_{0.5}O_4$.

P-$MgCr_{1.5}Mn_{0.5}O_4$	Mg_vac@*8a*	Mg_occ@*16c*	Inversion ratio (%)	*a* parameter (Å)
Pristine	*0*	*0*	*1.4*	*8.34362(5)*
Charged	*0.187(2)*	*0.0366(9)*	*1.4*	*8.31697(5)*
Discharged	*0.012(2)*	*0.016(1)*	*1.4*	*8.35220(6)*

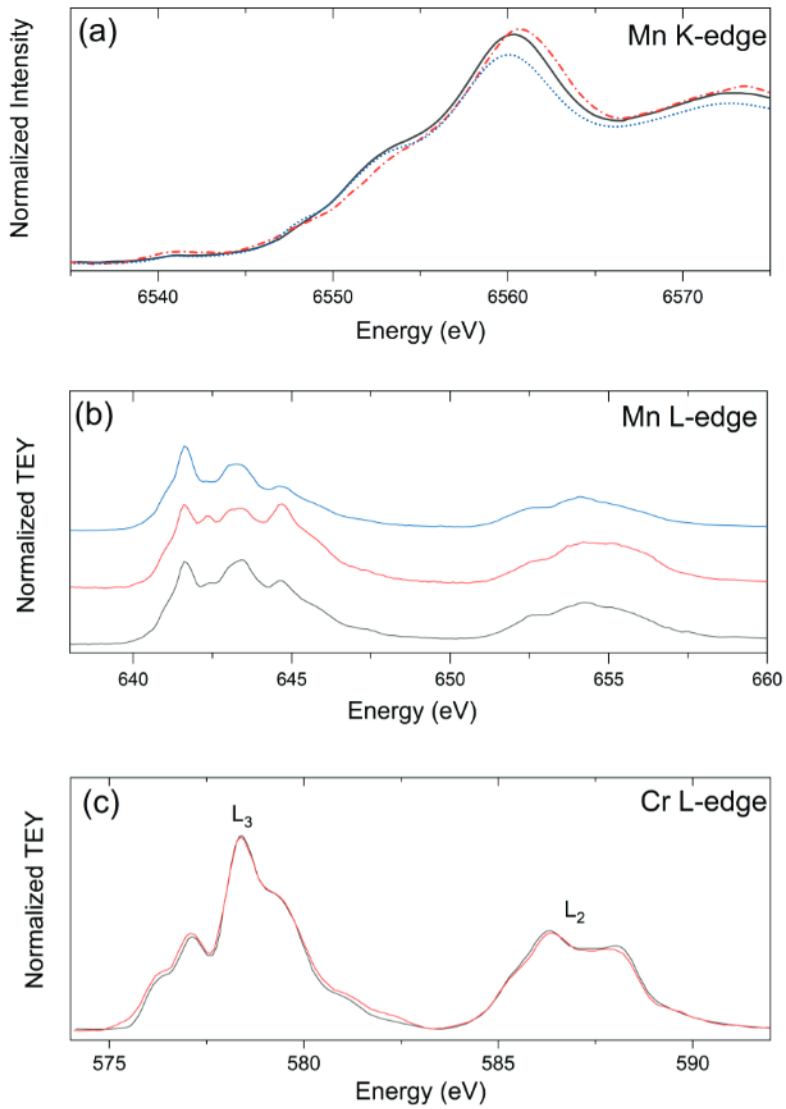

Figure 4. (a) Mn K-edge spectra of pristine (solid, black), charged (short dash, red) and discharged (short dot, blue) P-$MgCr_{1.5}Mn_{0.5}O_4$ electrodes. (b) Normalized Mn L-edge TEY spectra of pristine (black), charged (red) and discharged (blue) P-$MgCr_{1.5}Mn_{0.5}O_4$ electrodes. (c) Normalized Cr L-edge spectra of pristine (black) and charged P-$MgCr_{1.5}Mn_{0.5}O_4$ (red) collected in a TEY mode.

REFERENCES

1. Aurbach, D.; Lu, Z.; Schechter, A.; Gofer, Y.; Gizbar, H.; Turgeman, R.; Cohen, Y.; Moshkovich, M.; Levi, E., Prototype systems for rechargeable magnesium batteries. *Nature* **2000,** *407* (6805), 724-727.
2. Canepa, P.; Gautam, G. S.; Hannah, D. C.; Malik, R.; Liu, M.; Gallagher, K. G.; Persson, K. A.; Ceder, G., Odyssey of Multivalent Cathode Materials: Open Questions and Future Challenges. *Chem. Rev.* **2017,** *117* (5), 4287-4341.
3. Song, J.; Sahadeo, E.; Noked, M.; Lee, S. B., Mapping the Challenges of Magnesium Battery. *J. Phys. Chem. Lett.* **2016,** *7* (9), 1736-1749.
4. Levi, E.; Gofer, Y.; Aurbach, D., On the Way to Rechargeable Mg Batteries: The Challenge of New Cathode Materials. *Chem. Mater.* **2010,** *22* (3), 860-868.
5. Mao, M. L.; Gao, T.; Hou, S. Y.; Wang, C. S., A critical review of cathodes for rechargeable Mg batteries. *Chem. Soc. Rev.* **2018,** *47* (23), 8804-8841.
6. Gu, Y. P.; Katsura, Y.; Yoshino, T.; Takagi, H.; Taniguchi, K., Rechargeable magnesium-ion battery based on a $TiSe_2$-cathode with d-p orbital hybridized electronic structure. *Sci. Rep-Uk* **2015,** *5*, 12486.
7. Levi, E.; Gofer, Y.; Vestfreed, Y.; Lancry, E.; Aurbach, D., $Cu_2Mo_6S_8$ chevrel phase, a promising cathode material for new rechargeable Mg batteries: A mechanically induced chemical reaction. *Chem. Mater.* **2002,** *14* (6), 2767-2773.
8. Sun, X. Q.; Bonnick, P.; Duffort, V.; Liu, M.; Rong, Z. Q.; Persson, K. A.; Ceder, G.; Nazar, L. F., A high capacity thiospinel cathode for Mg batteries. *Energ. Environ. Sci.* **2016,** *9* (7), 2273-2277.
9. Liu, M.; Rong, Z. Q.; Malik, R.; Canepa, P.; Jain, A.; Ceder, G.; Persson, K. A., Spinel compounds as multivalent battery cathodes: a systematic evaluation based on ab initio calculations. *Energ. Environ. Sci.* **2015,** *8* (3), 964-974.
10. Rong, Z. Q.; Malik, R.; Canepa, P.; Gautam, G. S.; Liu, M.; Jain, A.; Persson, K.; Ceder, G., Materials Design Rules for Multivalent Ion Mobility in Intercalation Structures. *Chem. Mater.* **2015,** *27* (17), 6016-6021.
11. Arthur, T. S.; Zhang, R. G.; Ling, C.; Glans, P. A.; Fan, X. D.; Guo, J. H.; Mizuno, F., Understanding the Electrochemical Mechanism of K-alpha MnO_2 for Magnesium Battery Cathodes. *ACS Appl. Mater. Inter.* **2014,** *6* (10), 7004-7008.
12. Sun, X. Q.; Duffort, V.; Mehdi, B. L.; Browning, N. D.; Nazar, L. F., Investigation of the Mechanism of Mg Insertion in Birnessite in Nonaqueous and Aqueous Rechargeable Mg-Ion Batteries. *Chem. Mater.* **2016,** *28* (2), 534-542.
13. Wang, H.; Senguttuvan, P.; Proffit, D. L.; Pan, B. F.; Liao, C.; Burrell, A. K.; Vaughey, J. T.; Key, B., Formation of MgO during Chemical Magnesiation of Mg-Ion Battery Materials. *ECS Electrochem. Lett.* **2015,** *4* (8), A90-A93.
14. Bayliss, R. D. K., B.; Gautam, G. S.; Canepa, P.; Kwon, B. J.; Lapidus, S. H.; Dogan, F.; Adil, A. A.; Lipton, A. S.; Baker, P. J.; Ceder, G.; Vaughey, J. T.; Cabana, J, Probing Mg Migration in Spinel Oxides. *Chem. Mater.* **2020,** *32*, 663-670.
15. Chen, T. N.; Gautam, G. S.; Huang, W. X.; Ceder, G., First-Principles Study of the Voltage Profile and Mobility of Mg Intercalation in a Chromium Oxide Spinel. *Chem. Mater.* **2018,** *30* (1), 153-162.
16. Bob Jin Kwon, K.-C. L., Haesun Park, Yimin A. Wu, Krista L. Hawthorne, Haifeng Li, Soojeong K, Igor L. Bolotin, Timothy T. Fister, Peter Zapol, Robert F. Klie, Jordi Cabana, Chen

Liao, Saul H. Lapidus, Baris Key, John T. Vaughey, Probing Electrochemical Mg-Ion Activity in $MgCr_{2-x}V_xO_4$ Spinel Oxides. *Chem. Mater.* **2020**, *32*, 1162-1171.
17. Hu, L. H.; Jokisaari, J. R.; Kwon, B. J.; Yin, L.; Kim, S.; Park, H.; Lapidus, S. H.; Klie, R. F.; Key, B.; Zapol, P.; Ingram, B. J.; Vaughey, J. T.; Cabana, J., High Capacity for Mg^{2+} Deintercalation in Spinel Vanadium Oxide Nanocrystals. *ACS Energy Lett.* **2020,** *5* (8), 2721-2727.
18. Kwon, B. J.; Yin, L.; Park, H.; Parajuli, P.; Kumar, K.; Kim, S.; Yang, M. X.; Murphy, M.; Zapol, P.; Liao, C.; Fister, T. T.; Klie, R. F.; Cabana, J.; Vaughey, J. T.; Lapidus, S. H.; Key, B., High Voltage Mg-Ion Battery Cathode via a Solid Solution Cr-Mn Spinel Oxide. *Chem. Mater.* **2020,** *32* (15), 6577-6587.
19. Li, Z. Y.; Mu, X. K.; Zhao-Karger, Z.; Diemant, T.; Behm, R. J.; Kubel, C.; Fichtner, M., Fast kinetics of multivalent intercalation chemistry enabled by solvated magnesium-ions into self-established metallic layered materials. *Nat. Commun.* **2018,** *9*, 5115.
20. Gautam, G. S.; Canepa, P.; Urban, A.; Bo, S. H.; Ceder, G., Influence of Inversion on Mg Mobility and Electrochemistry in Spinels. *Chem. Mater.* **2017,** *29* (18), 7918-7930.
21. Burdett, J. K.; Price, G. D.; Price, S. L., Role of the Crystal-Field Theory in Determining the Structures of Spinels. *J. Am. Chem. Soc.* **1982,** *104* (1), 92-95.
22. Yin, L.; Kwon, B. J.; Choi, Y.; Bartel, C. J.; Yang, M.; Liao, C.; Key, B.; Ceder, G.; Lapidus, S. H., Operando X-ray Diffraction Studies of the Mg-Ion Migration Mechanisms in Spinel Cathodes for Rechargeable Mg-Ion Batteries. *J. Am. Chem. Soc.* **2021,** *143* (28), 10649-10658.
23. Bayliss, R. D.; Key, B.; Gautam, G. S.; Canepa, P.; Kwon, B. J.; Lapidus, S. H.; Dogan, F.; Adil, A. A.; Lipton, A. S.; Baker, P. J.; Ceder, G.; Vaughey, J. T.; Cabana, J., Probing Mg Migration in Spinel Oxides. *Chem. Mater.* **2020,** *32* (2), 663-670.
24. Yoo, H. D.; Jokisaari, J. R.; Yu, Y. S.; Kwon, B. J.; Hu, L. H.; Kim, S.; Han, S. D.; Loyez, M.; Lapidus, S. H.; Nolis, G. M.; Ingram, B. J.; Bolotin, I.; Ahmed, S.; Klie, R. F.; Vaughey, J. T.; Fister, T. T.; Cabana, J., Intercalation of Magnesium into a Layered Vanadium Oxide with High Capacity. *ACS Energy Lett.* **2019,** *4* (7), 1528-1534.
25. Lau, K. C.; Seguin, T. J.; Carino, E. V.; Hahn, N. T.; Connell, J. G.; Ingram, B. J.; Persson, K. A.; Zavadil, K. R.; Liao, C., Widening Electrochemical Window of Mg Salt by Weakly Coordinating Perfluoroalkoxyaluminate Anion for Mg Battery Electrolyte. *J. Electrochem. Soc.* **2019,** *166* (8), A1510-A1519.
26. Zhang, X. W.; Zunger, A., Diagrammatic Separation of Different Crystal Structures of A_2BX_4 Compounds Without Energy Minimization: A Pseudopotential Orbital Radii Approach. *Adv. Funct. Mater.* **2010,** *20* (12), 1944-1952.
27. Lee, J.; Seymour, L. D.; Pell, A. J.; Dutton, S. E.; Grey, C. P., A systematic study of Mg-^{25}NMR in paramagnetic transition metal oxides: applications to Mg-ion battery materials. *Phys. Chem. Chem. Phys.* **2017,** *19* (1), 613-625.
28. Ruch, P. W.; Cericola, D.; Hahn, M.; Kotz, R.; Wokaun, A., On the use of activated carbon as a quasi-reference electrode in non-aqueous electrolyte solutions. *J. Electroanal. Chem.* **2009,** *636* (1-2), 128-131.
29. Kim, C.; Phillips, P. J.; Key, B.; Yi, T. H.; Nordlund, D.; Yu, Y. S.; Bayliss, R. D.; Han, S. D.; He, M. N.; Zhang, Z. C.; Burrell, A. K.; Klie, R. F.; Cabana, J., Direct Observation of Reversible Magnesium Ion Intercalation into a Spinel Oxide Host. *Adv. Mater.* **2015,** *27* (22), 3377-3384.

30. Dau, H.; Liebisch, P.; Haumann, M., X-ray absorption spectroscopy to analyze nuclear geometry and electronic structure of biological metal centers - Potential and questions examined with special focus on the tetra-nuclear manganese complex of oxygenic photosynthesis. *Anal. Bioanal. Chem.* **2003,** *376* (5), 562-583.
31. Chen, Y. M.; Chen, C.; Zheng, C.; Dwaraknath, S.; Horton, M. K.; Cabana, J.; Rehr, J.; Vinson, J.; Dozier, A.; Kas, J. J.; Persson, K. A.; Ong, S. P., Database of ab initio L-edge X-ray absorption near edge structure. *Sci. Data* **2021,** *8* (1), 153.
32. Radharishnan, N. K.; Biswas, A. B., Neutron-Diffraction Study of Cation Migration in $MgMn_2O_4$. *Phys. Status. Solidi. A* **1976,** *37* (2), 719-&.
33. Yao, K. P. C.; Lu, Y. C.; Amanchukwu, C. V.; Kwabi, D. G.; Risch, M.; Zhou, J. G.; Grimaud, A.; Hammond, P. T.; Barde, F.; Shao-Horn, Y., The influence of transition metal oxides on the kinetics of Li_2O_2 oxidation in Li-O_2 batteries: high activity of chromium oxides. *Phys. Chem. Chem. Phys.* **2014,** *16* (6), 2297-2304.
34. Dedkov, Y. S.; Vinogradov, A. S.; Fonin, M.; Konig, C.; Vyalikh, D. V.; Preobrajenski, A. B.; Krasnikov, S. A.; Kleimenov, E. Y.; Nesterov, M. A.; Rudiger, U.; Molodtsov, S. L.; Guntherodt, G., Correlations in the electronic structure of half-metallic ferromagnetic CrO_2 films: An x-ray absorption and resonant photoemission spectroscopy study. *Phys. Rev. B* **2005,** *72* (6), 060401.
35. Hu, L. H.; Johnson, I. D.; Kim, S.; Nolis, G. M.; Freeland, J. W.; Yoo, H. D.; Fister, T. T.; McCafferty, L.; Ashton, T. E.; Darr, J. A.; Cabana, J., Tailoring the electrochemical activity of magnesium chromium oxide towards Mg batteries through control of size and crystal structure. *Nanoscale* **2019,** *11* (2), 639-646.